Available online at www.CivileJournal.org

Civil Engineering Journal

(E-ISSN: 2476-3055; ISSN: 2676-6957)

Vol. 11, No. 07, July, 2025

Experimental and Bearing Capacity Research on Prestressed Shape Memory Alloy Strips Confined Concrete Column

Lidan Xu [1, 2], Guangtao Mu [1, 2], Jitao Zhao [3], Miaomiao Zhu [1, 2], Ming Chen [1, 2], Yutong Yan [1], Mingfang Shi [1, 2*]

[1] *School of Civil Engineering, Inner Mongolia University of Science and Technology, Baotou 014010, China.*

[2] *Inner Mongolia Key Laboratory of Safety and Durability for Civil Engineering, Baotou 014010, China.*

[3] *School of Civil and Architecture Engineering, Panzhihua University, Panzhihua 617000, China.*

Received 09 April 2025; Revised 02 June 2025; Accepted 17 June 2025; Published 01 July 2025

Abstract

The prestressed shape memory alloy (SMA) strips confined columns are a novel reinforcement method, which not only exerts active confinement stress on the core concrete but also avoids the common stress hysteresis problem in reinforcement. This paper performed axial compression tests on eight sets of concrete columns with varying SMA strip width, net spacing, and pre-strain, and the impacts of these variables regarding the failure pattern, bearing capacity, and deformability of the specimens were investigated. A calculation model for the bearing capacity of SMA strips actively confined to concrete columns was established and contrasted with the prediction performance of the BP neural network. The results indicate that compared to the unconfined column, SMA strip-confined columns exhibit obvious ductile failure under compression, with the highest increase of bearing capacity and deformability reaching up to 20.27% and 24.96%, respectively. The confinement effect becomes better and better with the increasing strip width or the decreasing strip net spacing. When the strip pre-strain gradually increases, the bearing capacity of confined columns gradually improves, while the deformability first enhances and then weakens. The experimental data of other scholars is used to verify that the calculation results accord with the experimental results well, and the prediction precision of the proposed calculation model exceeds that of the BP neural network. Meanwhile, it is confirmed that the BP neural network exhibits a high fitting level in bearing capacity prediction ($R^2_{training}$=0.990 and R^2_{test}=0.965), offering a novel approach for predicting the bearing capacity of structures.

Keywords: Shape Memory Alloy Strips; Actively Confined; Uniaxial Compression; Bearing Capacity Calculation Model; BP Neural Network.

1. Introduction

As a critical load-bearing component in the building structural system, concrete columns play a significant role in bearing both vertical and lateral loads, with their mechanical properties directly affecting the stability and safety of the entire structure [1, 2]. However, due to the influence of multiple factors such as material aging, environmental erosion, human factors, and disaster effects, concrete structures frequently experience performance degradation, resulting in insufficient load-bearing capacity to meet the current code requirements. Therefore, it is urgent to take effective reinforcement and repair measures.

Traditional strengthening techniques primarily employ passive restraint mechanisms, including steel tube confined concrete [3, 4], fiber-reinforced polymer (FRP) confined concrete [5, 6], and high-strength spiral stirrup confined concrete [7]. Although these techniques can enhance the axial compressive performance of concrete columns to a certain extent, the stress lag effect is common during the strengthening process. To overcome these limitations, researchers have proposed active restraint reinforcement techniques, mainly including prestressed steel (such as steel strips [8-10] and

* Corresponding author: shimingfang2019@imust.edu.cn

http://dx.doi.org/10.28991/CEJ-2025-011-07-01

steel strands [11, 12]) and prestressed FRP [13-15]. The key advantage of this kind of technology lies in the application of preloading stress, which not only significantly improves the material utilization rate but also effectively alleviates the stress lag effect of the reinforced structure. However, steel has inherent defects such as easy corrosion and insufficient durability, while FRP materials rely on epoxy resin adhesives for surface bonding, which poses a risk of interface debonding. It is worth noting that the application of prestress for these two materials requires specialized tensioning equipment, resulting in complex construction techniques and high costs. Consequently, there are still many technical bottlenecks in the existing concrete column reinforcement technology. It is urgent to develop more efficient, economical, and reliable reinforcement solutions through technological innovation and method optimization.

Shape memory alloys (SMAs), as intelligent metallic materials, have attracted extensive attention in recent years [16-19]. Existing studies [20-22] have demonstrated that SMAs exhibit significant application potential in the active restraint reinforcement of concrete columns. Compared with traditional prestressed steel and prestressed FRP reinforcement techniques, the advantage of SMAs lies in that their prestress is achieved through the austenite-martensite phase transformation mechanism induced by thermal excitation, which provides a new technical path for structural reinforcement. Jung et al. [23] and Abdelrahman & El-Hacha [24] evaluated the mechanical properties of reinforced concrete (RC) columns strengthened with SMA wires and FRP under static and fatigue loading. It was found that active strengthening with SMA wires significantly improved the strength and stiffness of concrete columns more effectively than passive strengthening with FRP. Zerbe et al. [25], Chen & Andrawes [26], and Chen et al. [27] investigated the influence of various factors (like loading schemes, initial confining pressure, and external strip restraint ratio) on the compressive performance of SMA strips confined to concrete columns. The outcomes indicated that the active restraint effect of SMA strips remarkably enhances the axial bearing capacity and deformation capability. Based on experimental data, the corresponding finite element prediction model was further established [28, 29]. Moreover, Yeon et al. [30] explored the uniaxial compressive behavior of concrete columns confined by SMA spiral stirrups. The findings demonstrated that the activation of SMA spiral stirrups markedly improves the ductility of concrete columns, and the restraint effect is more pronounced when the stirrup spacing is smaller and the concrete strength is lower. Cui et al. [31] further examined the effects of prestress level, stirrup spacing, curing conditions, and concrete type on the performance of ultra-high-performance concrete (UHPC) columns reinforced with SMA spiral stirrups. The research found that the active restraint of SMA spiral stirrups effectively mitigates the brittleness of UHPC and significantly enhances the ultimate compressive strain of the specimens. Hong et al. [32] compared the influence of active and passive SMA restraints on the axial performance of large-scale concrete columns, finding that active restraint not only improves strength and ductility but also more effectively reduces concrete damage. Subsequently, Han et al. [33] compared the effects of different constraint methods (SMA active constraint, FRP passive constraint, and hybrid SMA-FRP constraint) on the performance of concrete columns under large eccentric compression. The results revealed that the active constraint with SMA strips was more effective in improving the bearing performance than the passive constraint with FRP. Moreover, the hybrid constraint of SMA and FRP exhibited a synergistic effect, further improving the structural performance.

The above-mentioned research has proved that SMA shows significant advantages in enhancing the bearing capacity and ductility performance of structural members. Currently, scholars at home and abroad have achieved relatively systematic results in the experimental research of SMA active reinforcement technology. However, there are still obvious deficiencies in the relevant theoretical analysis. Based on this research background, this study employs a combination of experimental research, theoretical analysis, and machine learning (ML) to explore the influence of different factors (SMA strip width, net spacing, and pre-strain) on the restraint effect of concrete columns, as illustrated in Figure 1. Firstly, the effects of different parameters on the failure mode, load-bearing capacity, and deformation capacity of SMA-strip-confined concrete columns were analyzed through experimental research. Subsequently, based on the experimental results and comprehensively considering the constraint effect of SMA strips on the core concrete, a bearing capacity calculation model with good applicability was established. Furthermore, to improve the computing efficiency and reduce the engineering application cost, the BP neural network method was introduced to predict the bearing characteristics of confined concrete columns and compared with the traditional calculation method. The research findings not only provide a theoretical foundation and technical guidance for SMA strengthening design in engineering practice but also open a new research approach for the prediction of structural bearing capacity.

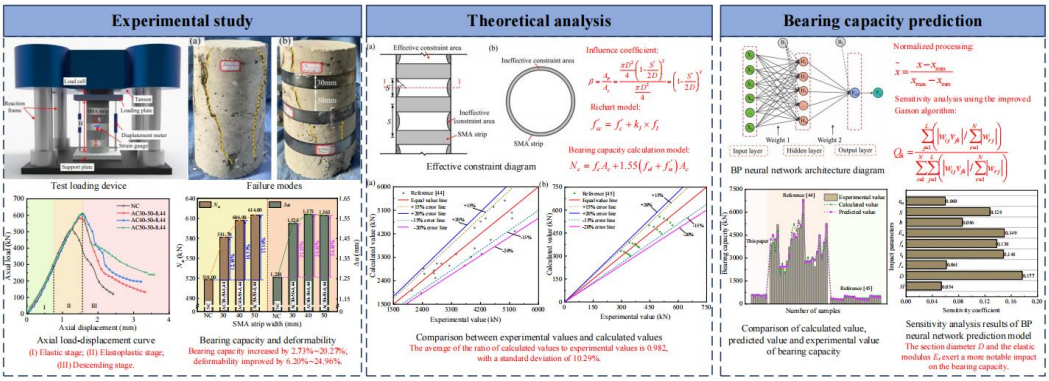

Figure 1. Schematic diagram of the research framework

2. Research Methodology

The steps for conducting this study are as follows: Firstly, the key parameters were determined, and the specimen preparation and loading scheme were described. Next, the failure modes of specimens under axial loading are analyzed, and the load-deflection curves as well as the variation laws of bearing capacity are investigated. Theoretically, by comparing various constraint models, the bearing capacity calculation formula of concrete columns confined by SMA strips was corrected and established based on the Richart model, and its reliability was verified. Meanwhile, the BP neural network is innovatively employed to predict the bearing capacity, and the influence degree of each factor is evaluated through parameter sensitivity analysis. Finally, the research conclusions are summarized. The technical flowchart shown in Figure 2.

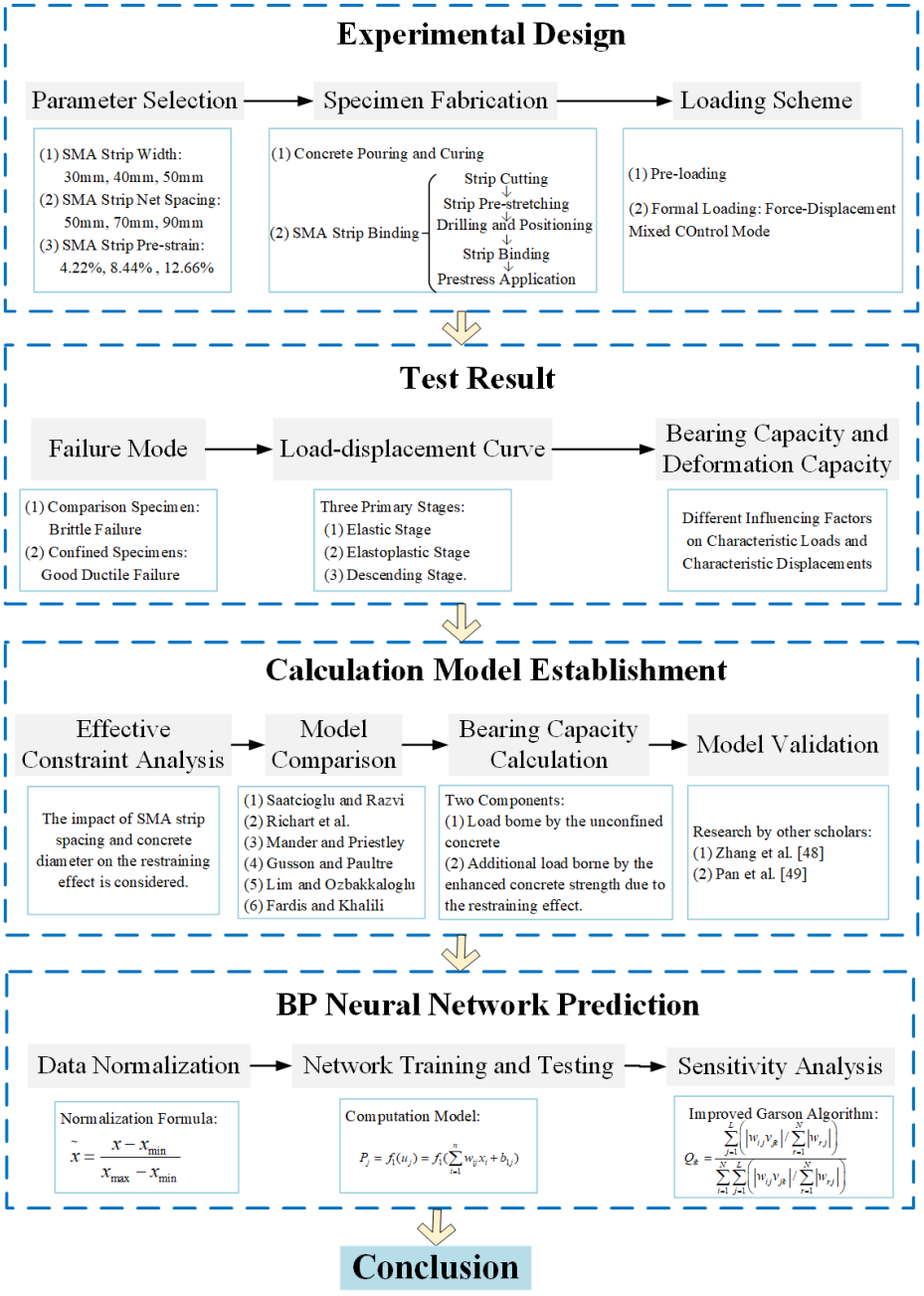

Figure 2. Flowchart of the research method

3. Experimental Overview

3.1. Material Properties

The experiment utilized commercial concrete with a strength grade of C30, and its mix proportion is detailed in Table 1. The specimens underwent curing under standard conditions (temperature 20±2℃, relative humidity≥95%) for 28 days. Three cubic specimens with dimensions of 150mm×150mm×150mm were reserved for the test. Based on GB/T 50081-2019 [34], its average cubic compressive strength is 33.31 MPa.

Table 1. Concrete mix proportion

Matrix strength	Water cement ratio	Water (kg/m^3)	Stone (kg/m^3)	Medium sand (kg/m^3)	Cement (kg/m^3)
C30	0.48	185	1255	586	385

In accordance with the standards of GB/T 39985-2021 [35] and GB/T 228.1-2021 [36], the SMA material was cut, ground and polished to prepare standard specimens with a gauge length of 60mm, a width of 30mm and a thickness of 0.5mm, as depicted in Figure 3-a. The uniaxial tensile test was performed using an electronic universal testing machine produced by Steel Yanak Testing Technology Co., Ltd. The loading process and failure mode are depicted in Figures 3-b and 3-c, respectively. The mechanical properties of the SMA strips measured are listed in Table 2.

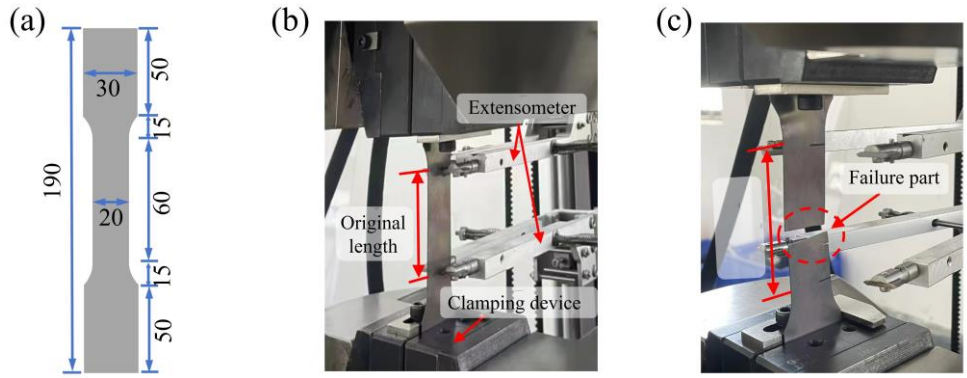

Figure 3. SMA standard sample and tensile test: (a) dimension of the standard sample (unit: mm); (b) the process of the tensile test; (c) the failure mode of the sample

Table 2. Mechanical properties of SMA strips

Yield strength (MPa)	Tensile strength (MPa)	Ultimate strain (%)	Elastic modulus (GPa)
167.0	1127.3	31.4	10.3

3.2. Specimen Design and Preparation

A total of 8 groups of specimens were designed for the experiment, with each group comprising 3 specimens prepared under the same conditions, amounting to 24 specimens in total. The primary variables investigated included the SMA strip width (30mm, 40mm and 50mm), the SMA strip net spacing (50mm, 70mm and 90mm) and the SMA strip pre-strain (4.22%, 8.44% and 12.66%). All specimens were fabricated using materials of the same specifications and batch, with dimensions of height H=300mm and diameter D=150mm. The detailed design parameters are provided in Table 3.

Table 3. Design parameters of specimens

Specimen number	SMA strip width b (mm)	SMA strip net spacing S' (mm)	SMA strip pre-strain ε_{is} (%)	Pre-stretching length Δl (mm)
NC	-	-	-	-
AC30-50-8.44	30	50	8.44	40
AC40-50-8.44	40	50	8.44	40
AC50-50-8.44	50	50	8.44	40
AC40-70-8.44	40	70	8.44	40
AC40-90-8.44	40	90	8.44	40
AC40-50-4.22	40	50	4.22	20
AC40-50-12.66	40	50	12.66	60

Note: NC denotes the comparison specimen without SMA strip confinement, while AC denotes the actively confined specimens. The specimen numbering follows the format of width-net spacing-pre-strain. For example, the number AC30-50-40 denotes that the specimen uses SMA strips with the width of 30mm, the net spacing of 50mm and the pre-strain of 4.22%. The pre-stretching length of the strip is calculated using the formula $\Delta l = l_0 \times \varepsilon_{is}$, where l_0 represents the original gauge length of the SMA strip, which is calculated as $l_0 = l - 2l_c = 560 - 2 \times 43 = 474mm$, where l denotes the total length of the strip, l_c corresponds to the length of the clamped portion by the fixture.

The fabrication of specimens primarily involves two key steps: concrete pouring and curing, and SMA strip binding. The focus lies on the SMA strip binding process, and the specific steps are as follows: (1) SMA strip cutting: According to the specimen size requirements, the SMA plates were cut into strips with a dimension of thickness × length = 0.5mm

× 560mm; (2) SMA strip pre-stretching: The SMA strips were pre-stretched using a universal testing machine. The corresponding stretching lengths for the specimens with pre-strain of 4.22%, 8.44% and 12.66% were 20mm, 40mm and 60mm, respectively, as shown in Figure 4-a. (3) Drilling and positioning: Based on the perimeter of the concrete column, the drilling positions at both ends of the SMA strips were pre-calculated and marked. A deep throat press machine was used to perform precise drilling at the marked locations, as shown in Figure 4-b. (4) SMA strip binding: At the overlapping part of the strips, anchorage connections were made using bolts with a diameter of 8mm and a length of 25mm, along with steel plates of 2mm thickness. The specific anchoring details are illustrated in Figure 4-c. (5) Prestress application: A hot gun was used to uniformly heat the SMA strips on the outer surface of the specimen (the hot gun should continuously and evenly heat the SMA surface for over five minutes to guarantee the alloy was sufficiently activated to recover). After heating, the SMA strip generated recovery stress due to its unique SME, thereby applying circumferential prestress to the concrete column before loading, as illustrated in Figure 4-d.

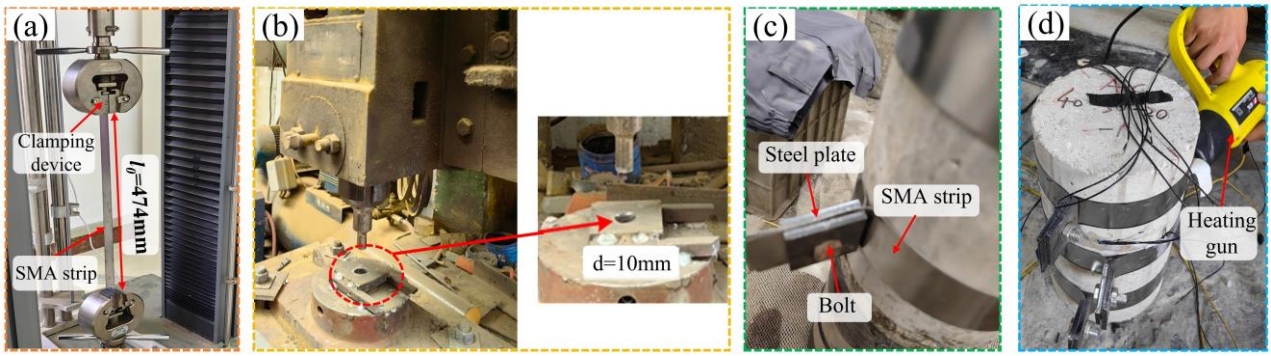

Figure 4. Binding process of SMA strips: (a) SMA strip pre-stretching; (b) drilling; (c) SMA strip binding; (d) activating SMA strip

3.3. Test Loading Device

The experiment was conducted on a 5000kN hydraulic testing machine, with the loading device presented in Figure 5. The loading process employed a force-displacement mixed control mode. Pre-loading was performed first to verify the normal operation of the instrument and eliminate the clearance between the specimen and the loading platform. During the formal loading phase, the load control with a rate of 20 kN/min was initially employed. Once the load attained the peak load, the displacement control with a rate of 0.1 mm/min was applied to continue loading until the specimen was damaged. During the test process, the axial displacement of the specimen was measured by two displacement meters positioned diagonally on the upper and lower loading plates, while the axial load was determined by the integrated data acquisition system of the testing machine.

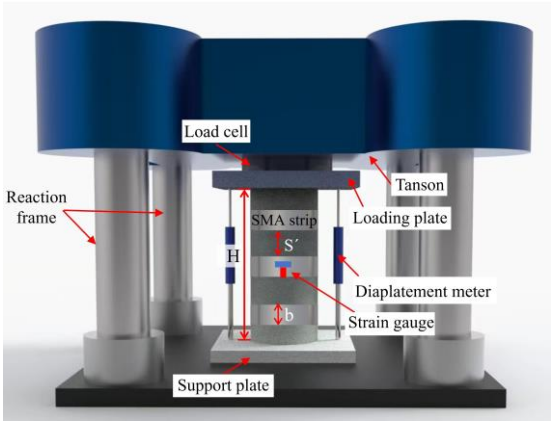

Figure 5. Test loading device

4. Results and Discussion

4.1. Failure Mode

4.1.1. Comparison Specimen NC

During the initial loading stage, no significant damage was observed on the surface of the specimen due to the relatively minor axial load. When the load rose to around 80% of the peak load, vertically inclined microcracks emerged at both ends of the column and propagated around it radially. With the load being continuously applied, the cracks progressively widened and spread towards the middle of the specimen, accompanied by the spalling of concrete debris.

When the load attained its peak, vertical cracks in the middle of the specimen rapidly propagated, forming an inverted conical failure surface, which led to a swift decline of its bearing capacity. Throughout the entire failure process, the NC specimen exhibited typical brittle failure characteristics, with no obvious warning signs prior to failure. The final failure pattern of the specimen is illustrated in Figure 6-a.

4.1.2. Confined Specimens

During the initial loading stage, the confined specimens were similar to the NC specimen, showing no significant visible changes, with the minimal deformation of the core concrete and the weak restraining effect of the SMA strips. As the load kept rising, the lateral deformation of the confined columns raised significantly and the concrete in the middle gradually expanded. The SMA strips began to exert the restraining effect, accompanied by a "popping" sound, and the slight cracks emerged on the concrete surface between the strips. Upon the load attaining approximately 80% of the peak load, the concrete around the cracks started to peel and crack. Once the peak load was attained, the concrete experienced localized crushing. Subsequently, the load showed a slow declining trend, and the concrete was further crushed and spalled, with the specimen being not completely crushed at the end of the experiment. Compared to the NC specimen, the confined columns exhibited cracking without fragmentation, showing good ductile failure characteristics, which is consistent with the research results of Choi et al. [37, 38] and Andrawes et al. [39]. The final failure modes of the specimens are illustrated in Figures 6-b to 6-h.

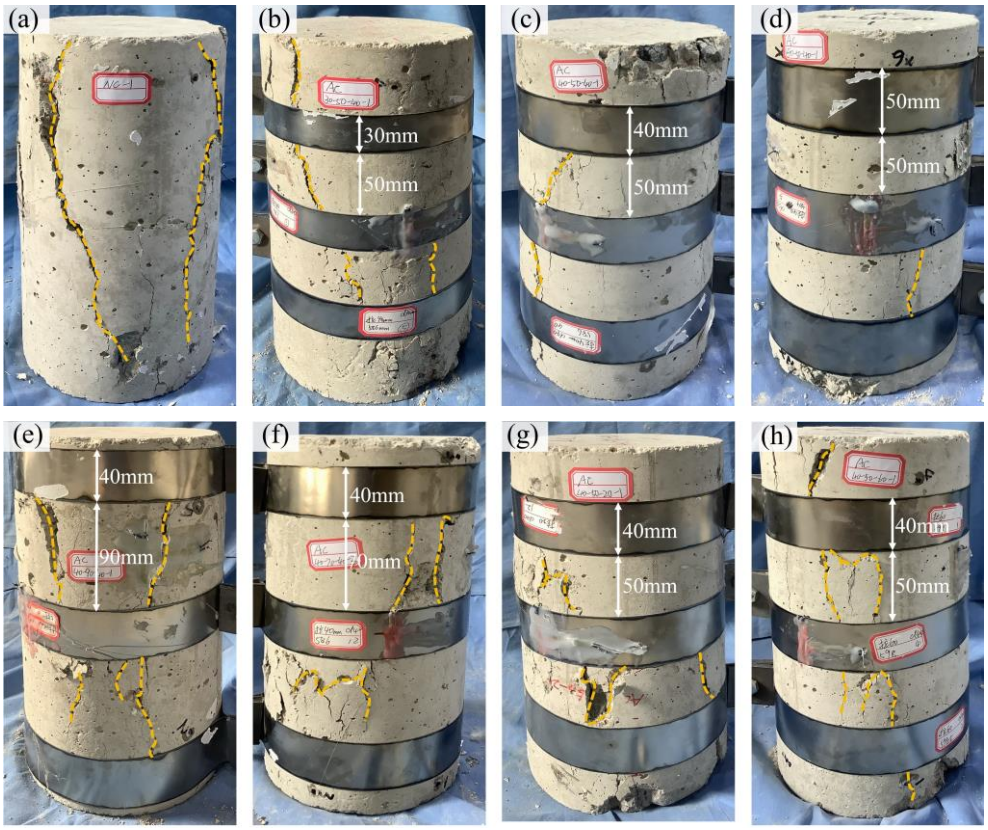

Figure 6. Failure modes of specimens: (a) NC; (b) AC30-50-8.44; (c) AC40-50-8.44; (d) AC50-50-8.44; (e) AC40-90-8.44; (f) AC40-70-8.44; (g) AC40-50-4.22; (h) AC40-50-12.66

As illustrated in Figure 4, the parameter setting of SMA strips has a significant impact on the final failure mode of the confined columns, which is specifically manifested in the following three aspects. (1) Effect of strip width: As the strip width increases, its restraining effect on the core concrete shows an obvious enhancement trend. The wider SMA strips not only more effectively suppressed the spalling of surface concrete but also markedly delayed the propagation of cracks, which can be clearly observed in Figures 6-b to 6-d. (2) Influence of strip net spacing: The reduction of the strip net spacing significantly improved the failure mode of the specimens. A smaller net spacing effectively slowed down the crack propagation rate in the concrete between the strips, thereby reducing the degree of concrete spalling. Consequently, specimens with smaller strip net spacing exhibited relatively lighter concrete spalling at failure, as illustrated in Figures 6-c, 6-e, and 6-f. (3) Effect of pre-strain: Increasing the pre-strain of the SMA strip enhanced its contact effect with the concrete interface, thereby significantly improving the restraining effect on the core concrete within the restraint zone. This enhanced restraint promoted the expansion of the concrete plastic zone, resulting in a more pronounced damage pattern at the final failure, as illustrated in Figures 6-c, 6-g, and 6-h.

4.2. Load-Displacement Curve

Figure 7 illustrates the axial load-displacement curves of specimens under varying influencing factors. As clearly observed in Figure 7, the load-displacement curves exhibited a similar trend, which is categorized into three primary stages: elastic stage, elastoplastic stage and descending stage. Taking the AC40-50-40 specimen as an example.

(I) Elastic stage. At this stage, there is a linear correlation between the load and displacement, and the curves of each specimen almost coincided. This phenomenon indicates that the restraining effect of the SMA strips is not pronounced because of the minimal lateral deformation of the concrete. However, the presence of SMA strips delays to some extent the initiation and propagation of microcracks within the specimen.

(II) Elastoplastic stage. When the load attained 50%~65% of the peak load, a distinct inflection point emerged on the load-displacement curve, marked by a declining slope of the curve. The reason is that when the load increased to a certain extent, the concrete underwent expansion deformation under the applied load, while the external SMA strips exerted a restraining effect on this deformation. During this process, tensile-shear friction was generated between the SMA strips and the surface of the concrete, causing the SMA strips to emit a "popping" sound.

(III) Descending stage. After attaining the ultimate bearing capacity, the load of the unconfined specimen exhibited a rapid decline, with a steep curve and limited deformation capacity in the later stage. In contrast, the bearing capacity of the confined specimens decreased relatively slowly, with a flatter curve and its ultimate deformation was significantly greater than that of the unconfined specimen. This clearly demonstrates that the restraining effect of SMA strips effectively improves the ductility of the concrete column, facilitating the transition from brittle failure to ductile failure

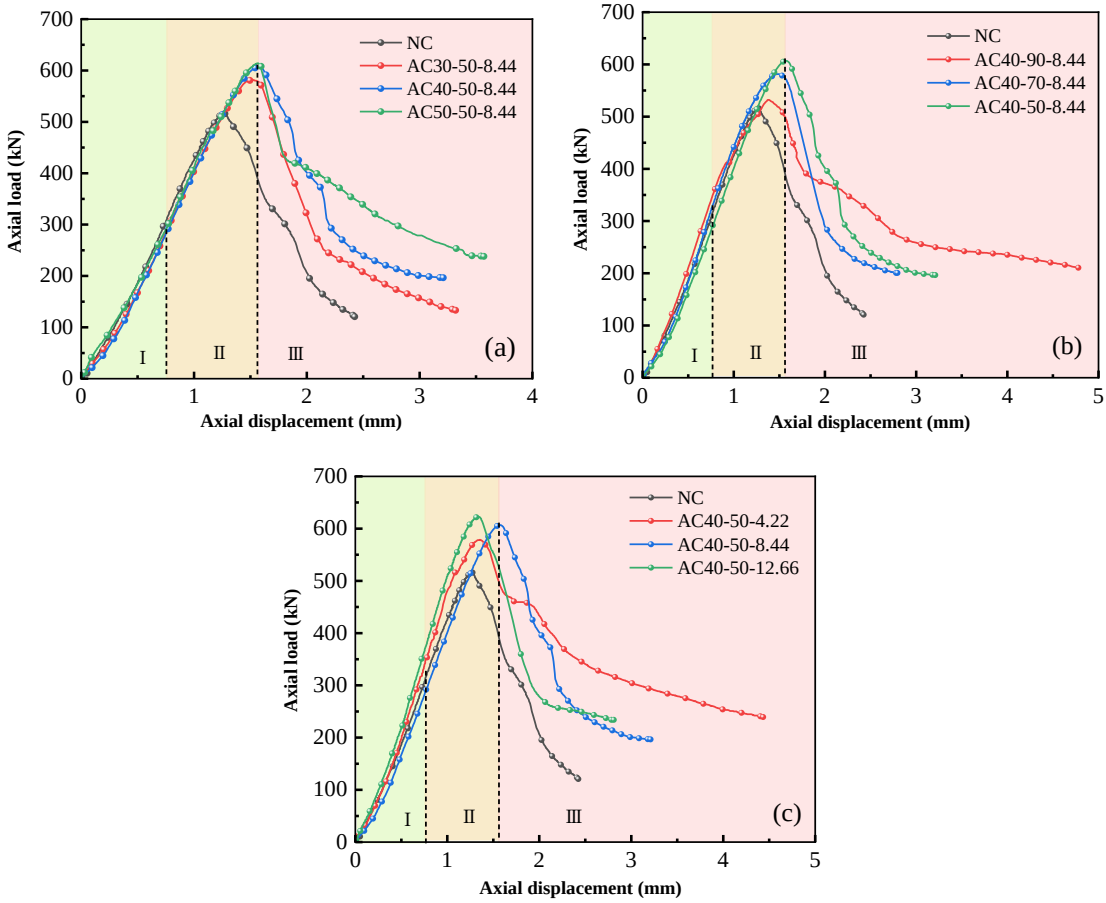

Figure 7. Load-displacement curve: (a) different SMA strip width; (b) different SMA strip net spacing; (c) different SMA strip pre-strain

4.3. Bearing Capacity and Deformability Performance Analysis

Table 4 presents the peak load and peak displacement of each specimen, where N_u represents the ultimate bearing capacity, Δu represents the peak displacement, which is the displacement corresponding to the peak load of the specimen. To quantitatively evaluate the influence of varying factors on the bearing capacity and deformability characteristics of confined columns, this study introduces two parameters: (1) Bearing capacity improvement coefficient K, which is expressed as $K = N_{ui}/N_{u0}$, where N_{ui} represents the ultimate bearing capacity of the confined columns and N_{u0}

represents the ultimate bearing capacity of the unconfined column. (2) Deformability improvement coefficient λ, which is expressed as $\lambda = \Delta u_i / \Delta u_0$, where Δu_i represents the peak displacement of the confined columns and Δu_0 represents the peak displacement of the unconfined column.

Table 4. The peak load and peak displacement of each specimen

Specimen number	N_u (kN)	K	Δu (mm)	λ
NC	518.00	1.000	1.258	1.000
AC30-50-8.44	581.70	1.123	1.525	1.212
AC40-50-8.44	606.90	1.172	1.571	1.249
AC50-50-8.44	614.00	1.185	1.565	1.244
AC40-70-8.44	532.12	1.027	1.341	1.066
AC40-90-8.44	581.33	1.122	1.481	1.177
AC40-50-4.22	578.67	1.117	1.353	1.076
AC40-50-12.66	623.00	1.203	1.336	1.062

As illustrated in Table 4, the specimens confined with prestressed SMA strips exhibited varying degrees of improvement in both ultimate bearing capacity and deformability characteristics compared to the NC specimen. Specifically, the bearing capacity increased by 2.73%~20.27% and the deformability improved by 6.20%~24.96%. This enhancement effect is primarily attributed to the self-prestress generated by the SMA strips under thermal activation, which allows the concrete to be subjected to initial lateral confining pressure before axial compression, thereby enabling the SMA strips to work in coordination with the concrete. During the loading process, internal cracks in the concrete gradually propagated and lateral deformation also increased as the continuously increasing load, resulting in the corresponding increase of restraining effect exerted by the SMA strips Meanwhile, this restraining effect effectively suppresses the further development of concrete cracks and enhances the ultimate compressive strain of the concrete, ultimately causing the improvement of the ultimate bearing capacity and deformability of the concrete. However, in the study of Tran et al. [40], the peak strength and ductility of the active restrained columns increased by 7% and 11%, respectively, whereas this study achieved a more significant improvement (with maximum increases in bearing capacity and deformation capacity reaching 20.27% and 24.96%, respectively). This can likely be attributed to the optimized design of the SMA strip width and pre-strain adopted in this study.

4.3.1. SMA Strip Width

By comparing the four groups of NC, AC30-50-8.44, AC40-50-8.44 and AC50-50-8.44 specimens, it can be observed that with the growing SMA strip width, the ultimate bearing capacity of the specimens rises, whereas the deformability presents a tendency of first rising and then gradually declining, as shown in Figure 8-a. When the SMA strip width is 30 mm, 40 mm and 50 mm, the ultimate bearing capacity enhances by 12.30%, 17.16% and 18.53%, and the deformability improves by 21.22%, 24.88% and 24.40% compared to the NC specimen. This improvement in mechanical performance is primarily attributed to the increased width of the SMA strip, which raises the volumetric stirrup ratio and thereby expands the contact area between the strips and the concrete matrix. Under the action of axial load, wider SMA strips exert a stronger restraining effect on the lateral expansion deformation of the concrete. Nevertheless, it is worth noting that when the strip width increases to 50mm, the deformation improvement coefficient of the specimen shows a slight decline. This phenomenon is explained as follows: under the condition of fixed strip spacing, overly wide strips significantly enhance the constraint effect on the end and middle areas of the concrete, which inhibits the full development of lateral deformation of the concrete to a certain extent. Consequently, although the increase of the SMA strip width effectively enhances the bearing capacity of concrete columns, there exists an optimal threshold for improving deformation performance. When the strip width exceeds a certain value, the improvement of the deformation capacity tends to be gentle, which aligns with the nonlinear growth law of the constraint effect proposed by Gusson & Paultre [41].

4.3.2. SMA Strip Net Spacing

By comparing the four groups of NC, AC40-90-8.44, AC40-70-8.44 and AC40-50-8.44 specimens, it is found that with a reduction in the SMA strip net spacing, the ultimate bearing capacity and deformability of the specimens show a progressive upward trend, as illustrated in Figure 8-b. When the SMA strip net spacing is 90 mm, 70 mm and 50 mm, the ultimate bearing capacity of the specimens increases by 2.73%, 12.23% and 17.16%, while the deformability improves by 6.60%, 17.73% and 24.88% compared to the NC specimen. This is primarily due to the enhanced restraint mechanism of SMA strips on the concrete. Specifically, compared to the strip-wrapped regions, the concrete in the inter-strip zones experiences relatively weaker constraint, resulting in relatively weaker sections within the specimen. Under

the axial loading, the failure of the specimen typically occurs first at these control sections with insufficient restraint. It is notable that as the strip net spacing decreases, the constraint effect on the strips on the core concrete is significantly enhanced. The smaller net spacing enables the SMA strips to form a denser restraint network, thereby more effectively restricting the lateral deformation of the concrete and suppressing the initiation and propagation of cracks. This strengthened constraint mechanism not only delays the failure process of the control section but also significantly improves the overall bearing capacity and deformation performance of the specimen by optimizing the stress distribution.

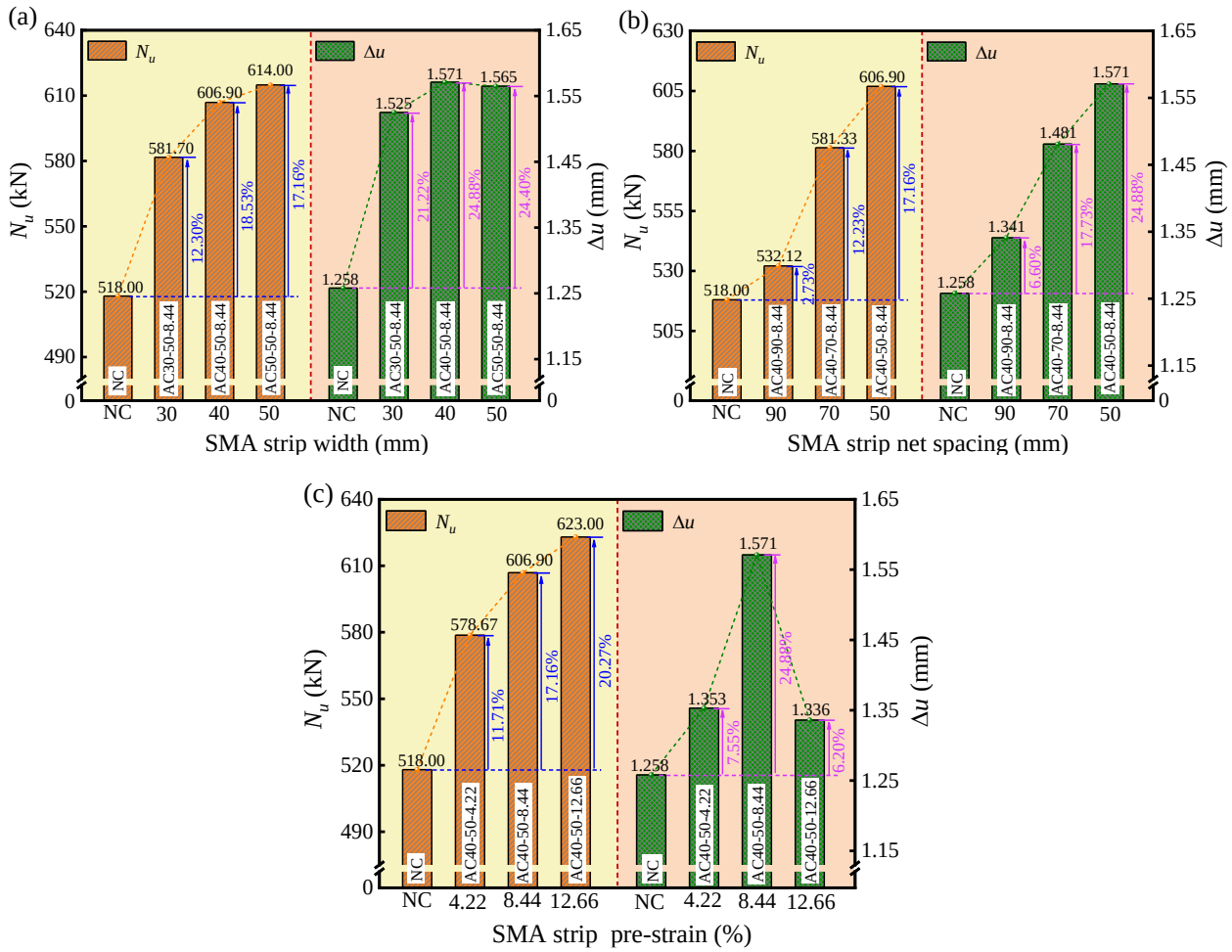

Figure 8. The influences of diverse influencing factors on bearing capacity and deformability: (a) different SMA strip width; (b) different SMA strip net spacing; (c) different SMA strip pre-strain

4.3.3. SMA Strip Pre-strain

By comparing the four groups of NC, AC40-50-4.22, AC40-50-8.44 and AC40-50-12.66 specimens, it is observed that as the SMA strip pre-strain increases, the ultimate bearing capacity of the specimens gradually improves, while the deformability first rises and then diminishes, as shown in Figure 8-c. When the SMA strip pre-strain is 4.22%, 8.44% and 12.66%, the ultimate bearing capacity of the specimens increases by 11.71%, 17.16% and 20.27%, while the deformability improves by 7.55%, 24.88% and 6.20% compared to the NC specimen. This is explained that with the increase of the SMA strip pre-strain, its lateral restraint effect on concrete exhibits a strengthening trend. This enhanced constrain not only significantly expands the plastic deformation area within the concrete but also promotes the homogenization of stress distribution. From the perspective of mechanical behavior, this restraint effect causes the specimen to enter the strengthening stage earlier, and effectively inhibits the initiation and expansion process of vertical cracks, thereby markedly improving the overall bearing capacity and deformation performance of the specimen. However, when the pre-strain reaches a value of 12.66%, the SMA material has exceeded its elastic deformation limit, resulting in incomplete shape recovery after thermal activation. This irreversible plastic deformation leads to a certain degree of attenuation of the constraint efficiency of SMA on concrete during the later loading stage, which results in a relatively limited increase in the deformation capacity of the specimen. This phenomenon agrees with the findings of Shin & Andrawes [42], who pointed out that excessive pre-strain may cause the SMA material to prematurely enter the plastic phase, thereby weakening its constraint effect.

5. Calculation Model of SMA Actively Confined Concrete Columns

5.1. Calculation Model of the Bearing Capacity

By applying thermal excitation to pre-stretched SMA strips using a hot air gun, self-prestress generated within the SMA strips exerts lateral confining pressure on the concrete, which effectively restricts the lateral deformation of the concrete and achieves active confinement. Due to the spacing between the SMA strips, the restraining effect along the column is non-uniform. Based on the "arch action" principle, the mid-region between two SMA strips is the weakest part of the specimen. Therefore, the cross-sectional area of this region is defined as the effective constraint area, as shown in Figure 9. To quantify the impact of SMA strip spacing and concrete diameter on the restraining effect, this paper introduces an influence coefficient β, and its expression is as follows:

$$\beta = \frac{A_p}{A_c} = \frac{\frac{\pi D^2}{4}\left(1-\frac{S'}{2D}\right)^2}{\frac{\pi D^2}{4}} = \left(1-\frac{S'}{2D}\right)^2 \quad (1)$$

where A_c denotes the cross-sectional area of the concrete column, A_p denotes the effective constraint area of the SMA strip, D denotes the diameter of the core concrete, S' denotes the net spacing of the SMA strip.

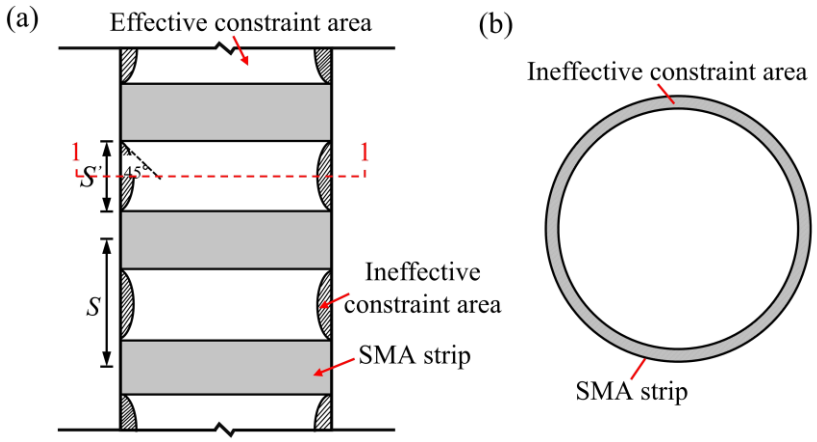

Figure 9. Effective constraint diagram: (a) circular column constrained with SMA strips; (b) cross section at 1-1

Table 5 shows the typical peak stress calculation model [41, 43-47]. The experimental data are substituted into each model for calculation, with the results presented in Table 6.

Table 5. Typical peak stress calculation model

Presenter	Calculation model
Saatcioglu & Razvi [43]	$f_{cc}^{'} = f_c^{'} + k_l \times f_l$, $k_l = 6.7(f_l)^{-0.17}$
Richart et al [44]	$f_{cc}^{'} = f_c^{'} + k_l \times f_l$, Richart recommends that k_l take 4.1
Mander et al. [45]	$f_{cc}^{'} = f_c^{'} \times \left(-1.254 + 2.254\sqrt{1+\frac{7.94f_l}{f_c^{'}}} - 2\frac{f_l}{f_c^{'}}\right)$
Gusson & Paultre [41]	$f_{cc}^{'} = f_c^{'} \times \left[1 + 2.1\left(\frac{f_l}{f_c^{'}}\right)^{0.7}\right]$
Lim & Ozbakkaloglu [46]	$f_{cc}^{'} = f_c^{'} + 5.2(f_c^{'})^{0.91}\left(\frac{f_l}{f_c^{'}}\right)^{(f_c^{'})^{-0.06}}$
Fardis and Khalili [47]	$f_{cc}^{'} = f_c^{'} \times \left[1 + 3.7\left(\frac{f_y t}{R f_c^{'}}\right)^{0.86}\right]$

Note: $f_{cc}^{'}$ denotes the peak stress of confined concrete, $f_c^{'}$ denotes the peak stress of comparison specimen, k_l denotes the coefficient of effective confinement stress, f_l denotes the effective confinement stress, f_y denotes the yield strength of the strengthening material, t denotes the thickness of the strengthening material, R denotes the radius of the concrete.

Table 6. Comparison of results of each model

Specimen number	The ratio of calculated values to experimental values from different references					
	Saatcioglu & Razvi [43]	Richart et al [44]	Mander et al. [45]	Gusson & Paultre [41]	Lim & Ozbakkaloglu [46]	Fardis & Khalili [47]
NC	-	-	-	-	-	-
AC30-50-8.44	1.112	1.029	1.105	1.080	1.126	1.088
AC40-50-8.44	1.067	0.986	1.059	1.035	1.079	1.043
AC50-50-8.44	1.054	0.975	1.047	1.023	1.067	1.031
AC40-70-8.44	1.113	1.030	1.106	1.081	1.127	1.089
AC40-90-8.44	1.217	1.125	1.208	1.181	1.231	1.190
AC40-50-4.22	1.118	1.034	1.111	1.085	1.132	1.094
AC40-50-12.66	1.042	0.964	1.035	1.011	1.055	1.019
Average value	1.103	1.035	1.096	1.071	1.117	1.079
Standard deviation	0.068	0.057	0.058	0.057	0.059	0.058
Coefficient of variation	0.062	0.055	0.053	0.053	0.053	0.05
Computational simplicity	Yes	Yes	No	Yes	Yes	Yes

Based on multiple factors such as the average value, standard deviation, coefficient of variation and computational simplicity of the results from various models, an appropriate base model was selected. After the comprehensive comparison, the Richart model from reference [44] was ultimately chosen as the base model for calculating the peak stress. On this foundation, the basic formula was modified by introducing influencing factors such as width, spacing and pre-strain, resulting in the following fitted expression:

$$f_{cc} = f_c + 1.55\left(f_{el} + f_{is}^{'}\right) \tag{2}$$

where f_{cc} denotes the strength of the confined concrete, f_c denotes the strength of the comparison specimen, f_{el} denotes the effective confinement stress of the SMA strip, $f_{el} = \beta \frac{2t_s f_s}{D}$, t_s denotes the thickness of the SMA strip, f_s denotes the yield stress of the SMA strip, D denotes the diameter of the core concrete, β denotes the influence coefficient, $f_{is}^{'}$ denotes the initial effective confinement stress of the prestressed SMA strip, $f_{is}^{'} = \beta \frac{2E_s \varepsilon_{is} T_s}{D}$, ε_{is} denotes the SMA strip pre-strain, T_s denotes the equivalent thickness of the SMA strip, $T_s = \frac{t_s b}{S}$, b and E_s are the width and elastic modulus of the SMA strip, respectively, S denotes the length from the center to the center of the SMA strip.

Based on theoretical analysis, the following basic assumptions are adopted when establishing the axial compression capacity calculation model. Firstly, it is assumed that the constraint stress of SMA strips on the same section is uniformly distributed. Secondly, the possible impact of the concrete softening effect is temporarily not considered. According to the principle of axial force balance of concrete columns, the axial compressive bearing capacity of SMA strip confined concrete columns comprises two components: the load borne by the unconfined concrete N_{c0} and the additional load borne by the enhanced concrete strength N_{cc} due to the restraining effect. Based on this, the expression for the axial bearing capacity N_c is as follows:

$$N_c = N_{c0} + N_{cc} = f_c A_c + (f_{cc} - f_c) A_c = f_c A_c + 1.55(f_{el} - f_{is}^{'}) A_c \tag{3}$$

5.2. Model Validation

The bearing capacity of each set of specimens was computed using Equation 3, and the results were contrasted with the experimental measured values. The specific data are presented in Table 7. The average value of the ratio between the calculated and the experimental values is 0.986, with the standard deviation of only 2.9%, which demonstrates that the calculation model has high precision and reliably predicts the bearing capacity of SMA strips confined concrete, thereby proving the validity of this calculation model.

Table 7. Comparison between experimental and calculated bearing capacity

Specimen number	Experimental value N_u (kN)	Calculated value N_c (kN)	N_c/N_u
NC	518.00	517.69	0.999
AC30-50-8.44	581.70	580.17	0.997
AC40-50-8.44	606.90	587.82	0.969
AC50-50-8.44	614.00	593.94	0.967
AC40-70-8.44	532.12	569.51	0.980
AC40-90-8.44	581.33	556.54	1.046
AC40-50-4.22	578.67	552.01	0.954
AC40-50-12.66	623.00	607.09	0.974
Average value	-	-	0.986
Standard deviation	-	-	0.029

To verify the applicability and practicality of the derived calculation model for the bearing capacity, the experimental data of actively confined concrete columns from Zhang et al. [48] and Pan et al. [49] (detailed in Appendix I; Table A1) were selected to validate the model. The comparison between the calculated and the experimental values is presented in Figure 10. The average value of the ratio of calculated to experimental values is 0.982, with the standard deviation of 10.29%. Among the data, 85% of the experimental results exhibit errors between the experimental and calculated values within ±15%, and almost all experimental data show errors within ±20%. In conclusion, the calculation model effectively fits the bearing capacity of actively confined concrete columns, demonstrating its high reliability and good applicability.

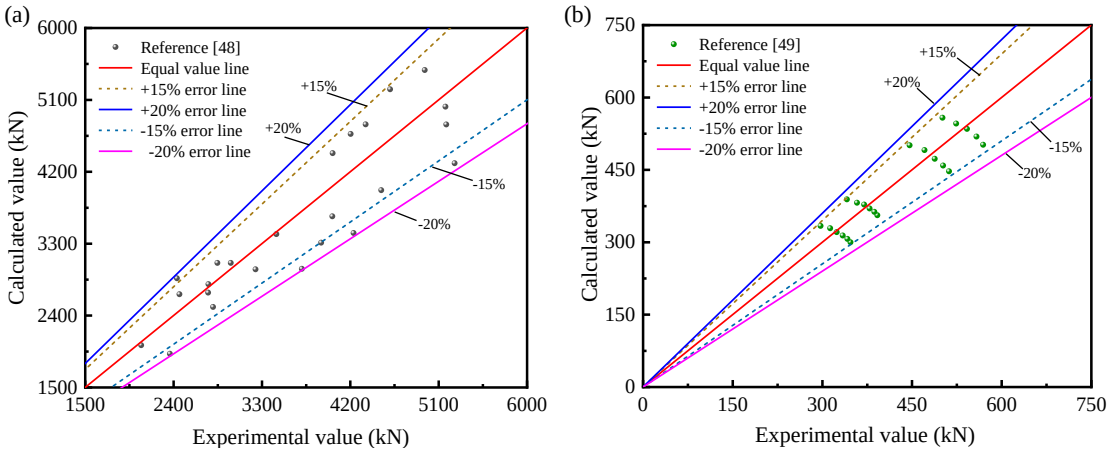

Figure 10. Comparison between experimental values and calculated values: (a) Zhang et al. [48]; (b) Pan et al. [49]

6. Prediction of Confined Concrete Columns Bearing Capacity Based on BP Neural Network

With the continuous in-depth research on confined concrete and its increasingly widespread engineering applications, scholars have proposed various methods for calculating the bearing capacity, which to some extent address the deficiencies and limitations in relevant theories and standards. However, due to the differences in the applicability of various calculation methods, there is a lack of a unified calculation theory for bearing capacity, which brings great difficulties to the scheme selection of engineering designers. In recent years, BP neural network, as an emerging computational approach, has provided new research perspectives and technical approaches to address this issue.

6.1. Principle of BP Neural Network

As a bionic computational model, the BP neural network simulates the basic characteristics of biological neural networks and is composed of multiple interconnected neuron units. This model effectively solves complex problems through the processing of input data and adaptive learning, serving as an efficient method for solving nonlinear problems [50-52]. Its training process is primarily achieved through the backpropagation algorithm, which inputs training samples into the network, and the weight is adjusted by comparing the deviation between the actual and desired outputs to minimize the error. Its advantage lies in the ability to effectively handle nonlinear problems, learn and memorize large amounts of data information, and it is widely applicable in various fields including pattern recognition, classification, prediction and control. The BP neural network is constituted of an input layer, a hidden layer and an output layer, with

each neuron receiving all outputs from the neurons in the previous layer and calculating its output through weight parameters and activation functions. The computation model P_j is shown in Equation 4, and the architecture of the BP neural network is illustrated in Figure 11.

$$P_j = f_1(u_j) = f_1(\sum_{i=1}^{n} w_{ij}x_i + b_{1j}) \quad (4)$$

where x_i represents the input value of node i of the input layer; w_{ij} represents the linking weight between input layer node i and hidden layer node j; b_{1j} represents the value of hidden layer node j; n represents the quantity of neurons within the input layer; and f_1 represents the transfer function existing between the input layer and the hidden layer.

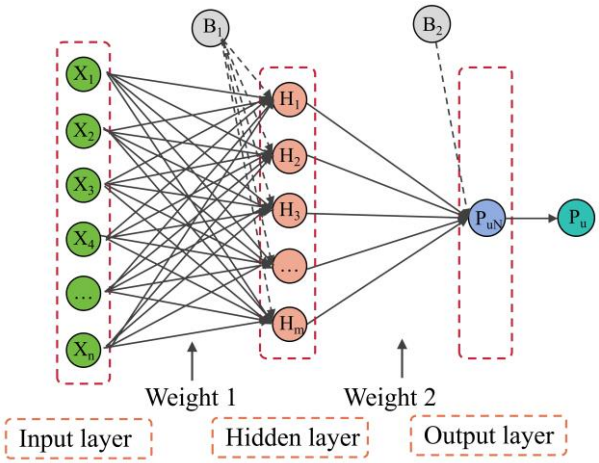

Figure 11. BP neural network architecture diagram

6.2. Model Establishment and Validation

6.2.1. Model Establishment

To validate the effectiveness of the BP neural network, this study collected experimental data from relevant literature [48, 49] and combined it with the data from 7 groups of specimens designed in this experiment to construct a database containing 49 groups of training samples. It is found from the Equation 3 that the section height H, the section diameter D, the compressive strength of the concrete cylinder f_c, the thickness of the constraint material t_s, the yield stress f_s, the elastic modulus E_s, the width b, the center-to-center spacing S, and the pre-strain ε_{is} all influence the bearing capacity of the component. Therefore, this section selects 9 different input parameters to establish the BP neural network. During the data processing stage, the dataset was partitioned into a training set and a test set at an 8:2 proportion, and finally 39 groups of training samples and 10 groups of test samples were obtained. To enhance the prediction accuracy of the network, the input and output data were normalized according to the Equation 5 [53], mapping them to the interval [-1, 1]. On this basis, the tansig transfer function was employed for the hidden layer, as well as the purelin transfer function was chosen for the output layer. The maximum number of training iterations was set to 1000, with the learning rate of 0.01 and the minimum training target error of $1e^{-6}$.

$$\tilde{x} = \frac{x - x_{min}}{xmin_{max}} \quad (5)$$

where x takes the input variable; x_{max} and x_{min} take the maximum and minimum values of the input variable; $\tilde{x}$ is the standardized input variables.

6.2.2. Model Validation

An in-depth investigation was conducted on the bearing capacity prediction performance of confined concrete samples using the BP neural network. The predicted values, calculated and experimental values of the samples were compared, as shown in Figure 12. It can be observed that for the experiments in this paper and those in Pan et al. [49], the calculated values are closer to the experimental values compared to the predicted values, with smaller error levels. However, for the experiments in Zhang et al. [48], the predicted values are closer to the experimental values than the calculated values, exhibiting relatively smaller errors. This indicates that the BP neural network effectively predicts the bearing capacity of confined concrete within the maximum value range of parameters, demonstrating superior computational ability. To quantitatively assess the accuracy of the calculated and predicted values, this study calculated the ratios of predicted values to experimental values and calculated values to experimental values, respectively, and introduced the following two parameters: (1) Mean. This parameter is used to describe the central tendency of the data

distribution and reflect the concentration characteristics of the data, helping to deeply understand the overall features of the data. (2) Variance. This parameter is used to quantify the degree of data dispersion, with a larger variance value indicating more significant fluctuations in the data. It is calculated that the mean and variance of the ratio between the calculated values and the experimental values are 0.981 and 0.096, respectively, while the mean and variance of the ratio between the predicted values and the experimental values are 0.956 and 0.100, respectively. The proposed computation model exhibits a smaller degree of dispersion compared to the experimental values, indicating that the model has low overall error and good predictive stability. Its computation accuracy is superior to the prediction outcomes of the BP neural network, thereby strongly demonstrating that the proposed computation mode has high accuracy. Notably, compared to the proposed computation model, the BP neural network exhibits relatively lower prediction accuracy for the bearing capacity. The main reason is that the number of training sample data is limited, which results in the generalization ability of the model failing to achieve the expected performance.

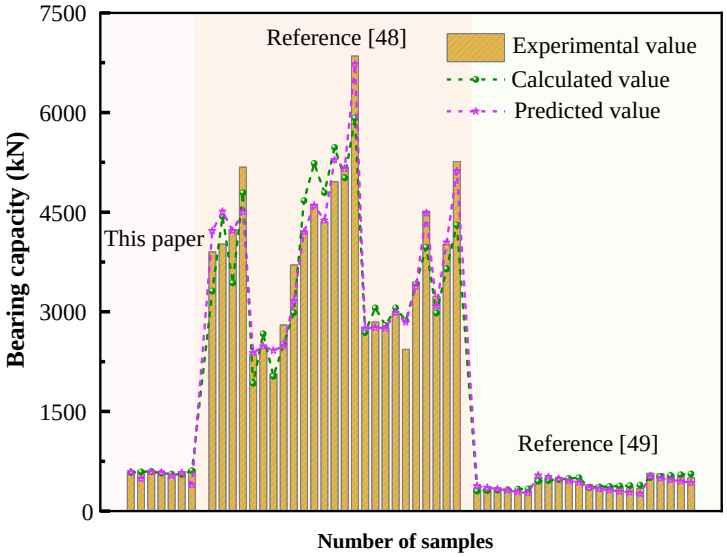

Figure 12. Comparison of calculated value, predicted value and experimental value of bearing capacity

In summary, the BP neural network has demonstrated excellent predictive performance in estimating the bearing capacity of confined concrete. The determination coefficients (R^2) of the training and test sets are 0.990 and 0.965, respectively, implying that the BP neural network has strong explanatory power for the bearing capacity of confined concrete and shows a high degree of fitting with the experimental values. Additionally, previous studies [54-56] have confirmed that the BP neural network is capable of effectively capturing the interaction relationships among the main influencing parameters, demonstrating good adaptability and serving as a reliable computational method. Therefore, with the continuous advancement of experimental research on confined concrete, new test specimens can be continuously added to improve the completeness of the learning sample dataset, thus further expanding the application of neural network analysis model in predicting the bearing capacity and enhancing the calculation accuracy.

6.3. Sensitivity Analysis

In the neural network analysis model, the training process iteratively optimizes the connection weights between the nodes of each hidden layer and the inter-layer threshold through the error backpropagation mechanism until the model meets the predetermined accuracy requirements, thereby establishing a nonlinear mapping relationship between input variables and output variables. Therefore, the connection weights and threshold parameters in the model play a crucial role in sensitivity analysis. This study employs the improved Garson algorithm [57] for parameter sensitivity analysis. Its basic principle lies in quantifying the relative contribution and influence degree of input variables on output variables by calculating the product of network weights between neurons in the hidden layers. The specific calculation method Q_{ik} is shown in Equation 6.

$$Q_{ik} = \frac{\sum_{j=1}^{L}\left(\left|w_{ij}v_{jk}\right|/\sum_{r=1}^{N}\left|w_{rj}\right|\right)}{\sum_{i=1}^{N}\sum_{i=1}^{L}\left(\left|w_{ii}v_{ik}\right|/\sum_{r=1}^{N}\left|w_{ri}\right|\right)} \quad (6)$$

where w_{ij} represents the network weight between the i-th input node and the j-th hidden node, with N input nodes and L hidden nodes; v_{jk} represents the mesh weight between the j-th hidden node and the k-th output node; $\sum_{r=1}^{N}\left|w_{rj}\right|$ represents the absolute value of the mesh weight between all input nodes and the j-th hidden node. The purpose of taking the absolute value lies in removing the issue of positive and negative cancellation in the network weight synthesis formula.

Figure 13 reveals the contribution values of 9 input variables (H, D, f_c, t_s, f_s, E_s, b, S, ε_{is}) to the output variable (the bearing capacity N_c). It can be observed that the concrete column parameters (H, D and f_c) and the constraint material parameters (t_s, f_s, E_s, b, S and ε_{is}) exert a certain impact on the bearing capacity. Moreover, the sensitivity coefficients of each influencing factor are sequenced as follows: $D > E_s > t_s > f_s > S > b > f_c > \varepsilon_{is} > H$, as shown in Table 8. The sensitivity coefficients of the five input parameters (D, E_s, t_s, f_s and S) all exceed 0.1, indicating that they present a notable influence on the bearing capacity of the confined concrete column. Of these, the section diameter D and elastic modulus E_s have the most remarkable contribution to the bearing capacity, with a sensitivity coefficient of 0.177 and 0.149, respectively. Therefore, the influence of parameters such as D, E_s, t_s, f_s and S on the bearing capacity can be considered in future research. Moreover, a multivariate mathematical relationship between these variable indexes and the bearing capacity can be established to adequately reflect the mechanical behaviour of the structure during service. However, the width b and pre-strain level ε_{is} are also concerned influencing parameters in the experiment, the analysis results indicate that the sensitivity coefficient is low. The reason is that the test dataset of the confined concrete columns is small, which leads to a small degree of influence of these two parameters on the bearing capacity. Further research needs to expand more effective learning samples to optimize this model.

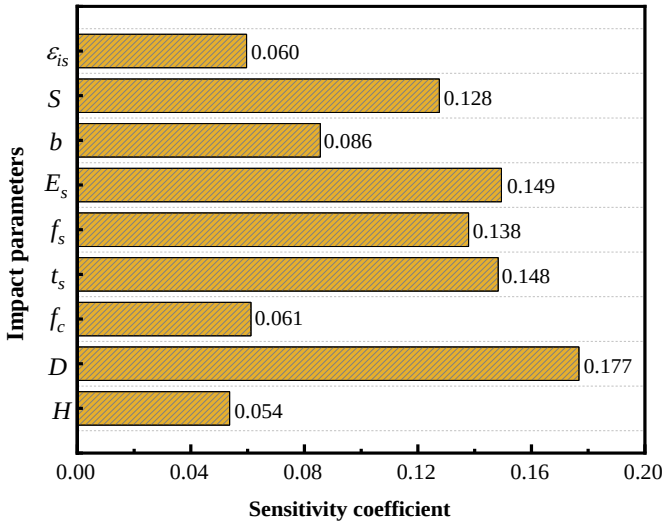

Figure 13. Sensitivity analysis results of neural network prediction model

Table 8. Ranking of the sensitivity coefficients of each influencing factor

Input variable	Sensitivity coefficient	Ranking of influence degree
Section diameter D	0.177	1
Elastic modulus E_s	0.149	2
Thickness of the constraint material t_s	0.148	3
Yield stress f_s	0.138	4
Center-to-center spacing S	0.128	5
Width b	0.086	6
Compressive strength of the concrete f_c	0.061	7
Pre-strain ε_{is}	0.060	8
Section height H	0.054	9

7. Conclusions

In this paper, the axial compression behaviour of concrete confined by prestressed SMA strips is explored through experiments and theoretical analysis. The findings are presented as follows:

- Prestressed SMA strips are capable of exerting the lateral confining force on concrete, thereby providing effective confinement. The specimen experiences a state of triaxial compression under axial loading, which retards the initiation and propagation of cracks and transforms the failure mode of the concrete from brittle to ductile.
- The bearing capacity and deformability of the specimen are remarkably raised with the increasing SMA strip width and the decreasing net spacing. However, as the strip pre-strain grows, the deformability of the specimen initially rises and then declines. This is primarily because when the pre-strain is 12.66%, the SMA strips exceed the elastic deformation zone and fail to fully recover after activation, leading to a reduction in the restraining effect of the SMA strips during the later stages of loading.

- This paper establishes a bearing capacity computation model regarding the SMA strips actively restrained concrete. The comparison with experimental data from other scholars demonstrates that the calculated values obtained by the proposed model align well with the experimental values, indicating its high applicability and providing a reliable reference for engineering design applications.
- The BP neural network is employed to estimate the bearing capacity of confined concrete columns, which proves its good fit with the test results ($R^2_{training}$=0.990 and R^2_{test}=0.965), as well as its feasibility and validity in bearing capacity prediction. On this basis, the improved Garson algorithm is employed to compute the sensitivity coefficient of the input variables, revealing that the section diameter D and the elastic modulus E_s exert a more notable influence on the bearing capacity.

8. Declarations

8.1. Author Contributions

Conceptualization, L.D.X. and J.T.Z.; methodology, M.M.Z. and Y.T.Y.; software, G.T.M.; validation, J.T.Z.; formal analysis, G.T.M.; investigation, M.M.Z. and Y.T.Y.; resources, M.C. and M.F.S.; data curation, J.T.Z.; writing—original draft preparation, G.T.M.; writing—review and editing, L.D.X.; visualization, M.M.Z. and Y.T.Y.; supervision, L.D.X.; project administration, M.C. and M.F.S.; funding acquisition, M.C. and M.F.S. All authors have read and agreed to the published version of the manuscript.

8.2. Data Availability Statement

The data presented in this study are available on request from the corresponding author.

8.3. Funding

This study was supported by the National Natural Science Foundation of China (No. 52168024; No. 52468026), the Natural Science Foundation of Inner Mongolia Autonomous Region (No. 2024MS05066), the Fundamental Research Funds for Inner Mongolia University of Science & Technology (No. 2023YXXS033; No. 2023YXXS034; No. 2024YXXS042; No. 2024YXXS066).

8.4. Acknowledgements

The authors would like to thank the Inner Mongolia University of Science and Technology Innovation Fund Project, and the Quality and Efficiency Improvement Project of the Civil Engineering Discipline.

8.5. Conflicts of Interest

The authors declare no conflict of interest.

9. References

[1] Cheng, S., Han, J., & He, H. (2025). Experimental, theoretical and numerical studies of damaged RC columns repaired with modified concrete and textile. Construction and Building Materials, 466, 140328. doi:10.1016/j.conbuildmat.2025.140328.

[2] Xu, R., Chen, Z., & Ning, F. (2025). Axial compression mechanism and numerical analysis of CFRP-PVC tube and I-shaped steel composite confined concrete column. Construction and Building Materials, 461, 139931. doi:10.1016/j.conbuildmat.2025.139931.

[3] He, F., Li, C., Chen, B., Briseghella, B., & Xue, J. (2024). Axial compression behavior of steel tube reinforced concrete column. Engineering Structures, 303, 117548. doi:10.1016/j.engstruct.2024.117548.

[4] Bui, V. T., & Kim, S. E. (2021). Nonlinear inelastic analysis of semi-rigid steel frames with circular concrete-filled steel tubular columns. International Journal of Mechanical Sciences, 196, 106273. doi:10.1016/j.ijmecsci.2021.106273.

[5] Li, H., Wei, Y., Hu, Y., Zhao, L., Wang, G., & Zhang, Y. (2024). Experimental and theoretical analysis of FRP-confined square lightweight aggregate concrete columns under axial compression. Case Studies in Construction Materials, 20, 2982. doi:10.1016/j.cscm.2024.e02982.

[6] Zeng, J. J., Ye, Y. Y., Liu, W. Te, Zhuge, Y., Liu, Y., & Yue, Q. R. (2023). Behaviour of FRP spiral-confined concrete and contribution of FRP longitudinal bars in FRP-RC columns under axial compression. Engineering Structures, 281(15), 115747. doi:10.1016/j.engstruct.2023.115747.

[7] Zhou, C., Chen, Z., Shi, S. Q., & Cai, L. (2018). Behavior of concrete columns confined with both steel angles and spiral hoops under axial compression. Steel and Composite Structures, 27(6), 747–759. doi:10.12989/scs.2018.27.6.747.

[8] Si, J., Wu, L., & Guo, W. (2021). Axial compression of reinforced concrete columns strengthened by composite of prestressed plastic-steel strip and angle steel: An experimental study. Structural Concrete, 22(6), 3620–3629. doi:10.1002/suco.202000786.

[9] Wang, H., Zhou, X., & Wang, L. (2019). Experimental investigation of damaged circular reinforced concrete columns with pre-tensioned steel hoops. Engineering Structures, 197, 109384. doi:10.1016/j.engstruct.2019.109384.

[10] Verderame, G. M., Ricci, P., De Risi, M. T., & Del Gaudio, C. (2022). Experimental response of unreinforced exterior RC joints strengthened with prestressed steel strips. Engineering Structures, 251, 113358. doi:10.1016/j.engstruct.2021.113358.

[11] Yan-xia, Z., Zhe-wen, H., Yang-long, L., Bo-wen, J., Xiao-tian, C., & Meng-yao, C. (2022). Experimental and numerical investigation of prefabricated prestressed vertical steel strand core tube flange column connection joint. Journal of Constructional Steel Research, 190, 107124. doi:10.1016/j.jcsr.2021.107124.

[12] Wei, Y., Xu, P., Zhang, Y., Wang, G., & Zheng, K. (2022). Compressive behaviour of FRP-steel wire mesh composite tubes filled with seawater and sea sand concrete. Construction and Building Materials, 314, 7763. doi:10.1016/j.conbuildmat.2021.125608.

[13] Chen, C., Fang, H., Lim, Y. M., Xie, H., Chen, J., & Park, J. W. (2025). Experimental and numerical studies on compressive behavior of winding FRP grid spiral stirrups confined circular concrete columns. Composites Part A: Applied Science and Manufacturing, 191, 108709. doi:10.1016/j.compositesa.2025.108709.

[14] Wang, Z., Li, Z., & Feng, P. (2023). Cyclic axial compressive performance of the RC columns reinforced with FRP confined concrete core encased rebar. Engineering Structures, 274, 115166. doi:10.1016/j.engstruct.2022.115166.

[15] Wang, D., Gu, J., Tao, Y., & Shi, Q. (2025). Axial compression behavior of FRP confined steel reinforced UHPC column. Engineering Structures, 328, 119747. doi:10.1016/j.engstruct.2025.119747.

[16] Shi, M., Xu, G., Zhao, J., & Xu, L. (2024). The study on bond-slip constitutive model of shape memory alloy fiber-reinforced concrete. Construction and Building Materials, 418, 135395. doi:10.1016/j.conbuildmat.2024.135395.

[17] Xu, L., Zhu, M., Zhao, J., Shi, M., & Chen, M. (2025). Study on axial compressive damage performance of SMA strips confined concrete columns by acoustic emission technology. Smart Materials and Structures, 34(2), 25038. doi:10.1088/1361-665X/adabcc.

[18] Xu, L., Zhu, M., Zhao, J., Chen, M., & Shi, M. (2025). Axial stress-strain behavior of shape memory alloy strips constrained concrete columns. Structures, 72, 10822. doi:10.1016/j.istruc.2025.108225.

[19] Qian, H., Yang, M. T., Shi, Y., Ye, Y. X., & Wu, B. (2025). Research on the seismic performance of self-centering concrete-filled superelastic Cu-based SMA tube columns. Structures, 74, 108516. doi:10.1016/j.istruc.2025.108516.

[20] Molod, M. A., Spyridis, P., & Barthold, F. J. (2022). Applications of shape memory alloys in structural engineering with a focus on concrete construction – A comprehensive review. Construction and Building Materials, 337, 127565. doi:10.1016/j.conbuildmat.2022.127565.

[21] Liu, Z., Zhu, H., Zeng, Y., Dong, Z., Ji, J., Wu, G., & Zhao, X. (2024). Study on the flexural properties of T-shaped concrete beams reinforced with iron-based shape memory alloy rebar. Engineering Structures, 306, 117792. doi:10.1016/j.engstruct.2024.117792.

[22] Hong, H., Gencturk, B., Saiidi, M. S., Zheng, B., & Pan, X. (2025). Seismic performance of self-centering columns post-tensioned with iron-based shape memory alloy (FeSMA) bars. Engineering Structures, 334, 12021. doi:10.1016/j.engstruct.2025.120218.

[23] Jung, D., Wilcoski, J., & Andrawes, B. (2018). Bidirectional shake table testing of RC columns retrofitted and repaired with shape memory alloy spirals. Engineering Structures, 160, 171–185. doi:10.1016/j.engstruct.2017.12.046.

[24] Abdelrahman, K., & El-Hacha, R. (2020). Analytical prediction model for circular SMA-confined reinforced concrete columns. Engineering Structures, 213, 110547. doi:10.1016/j.engstruct.2020.110547.

[25] Zerbe, L., Vieira, D., Belarbi, A., & Senouci, A. (2022). Uniaxial compressive behavior of circular concrete columns actively confined with Fe-SMA strips. Engineering Structures, 255, 113878. doi:10.1016/j.engstruct.2022.113878.

[26] Chen, Q., & Andrawes, B. (2017). Cyclic Stress–Strain Behavior of Concrete Confined with NiTiNb-Shape Memory Alloy Spirals. Journal of Structural Engineering, 143(5), 4017008. doi:10.1061/(asce)st.1943-541x.0001728.

[27] Chen, Q., Shin, M., & Andrawes, B. (2014). Experimental study of non-circular concrete elements actively confined with shape memory alloy wires. Construction and Building Materials, 61, 303–311. doi:10.1016/j.conbuildmat.2014.02.076.

[28] Vieira, D., Zerbe, L., & Belarbi, A. (2023). Numerical modeling of iron-based SMA confined concrete columns under axial compressive loading. Engineering Structures, 275, 115185. doi:10.1016/j.engstruct.2022.115185.

[29] Chen, Q., & Andrawes, B. (2017). Plasticity Modeling of Concrete Confined With NiTiNb Shape Memory Alloy Spirals. Structures, 11, 1–10. doi:10.1016/j.istruc.2017.03.006.

[30] Yeon, Y., Ji, S., & Hong, K. (2024). Uniaxial compressive behavior of concrete column actively confined with internal Fe-SMA spirals. Construction and Building Materials, 418, 135393. doi:10.1016/j.conbuildmat.2024.135393.

[31] Cui, C., Dong, Z., Zhu, H., Zhao, Y., Han, T., Pan, Y., & Ghafoori, E. (2025). Axial compressive behavior of UHPC columns reinforced with self-prestressed Fe-SMA spiral stirrups. Structures, 77, 109107. doi:10.1016/j.istruc.2025.109107.

[32] Hong, H., Gencturk, B., Belarbi, A., & Vieira, D. (2025). Active confinement of large-scale reinforced concrete columns using iron-based shape memory alloy (FeSMA) strips. Journal of Building Engineering, 108, 12848. doi:10.1016/j.jobe.2025.112848.

[33] Han, T., Dong, Z., Zhu, H., Cui, C., & Zhao, O. (2025). Compression performance of FRP externally wrapped Fe-SMA strips confined concrete columns under large eccentric load. Structures, 74, 108554. doi:10.1016/j.istruc.2025.108554.

[34] GB/T 50081-2019. (2019). Standard for test methods of concrete physical and mechanical properties. Ministry of Housing and Urban Rural Development, Beijing, China.

[35] GB/T 39985-2021. (2021). Titanium-nickel shape memory alloy plate. State Administration for Market Regulation and Standardization Administration. Ministry of Housing and Urban Rural Development, Beijing, China.

[36] GB/T 228.1-2021. (2021). Metallic Materials-Tensile testing-Part 1: Method of test at room temperature. State Administration for Market Regulation and Standardization Administration. Ministry of Housing and Urban Rural Development, Beijing, China.

[37] Choi, E., Chung, Y. S., Cho, B. S., & Nam, T. H. (2008). Confining concrete cylinders using shape memory alloy wires. European Physical Journal: Special Topics, 158(1), 255–259. doi:10.1140/epjst/e2008-00684-0.

[38] Choi, E., Nam, T. H., Cho, S. C., Chung, Y. S., & Park, T. (2008). The behavior of concrete cylinders confined by shape memory alloy wires. Smart Materials and Structures, 17(6), 65032. doi:10.1088/0964-1726/17/6/065032.

[39] Andrawes, B., Shin, M., & Wierschem, N. (2010). Active Confinement of Reinforced Concrete Bridge Columns Using Shape Memory Alloys. Journal of Bridge Engineering, 15(1), 81–89. doi:10.1061/(asce)be.1943-5592.0000038.

[40] Tran, H., Balandraud, X., & Destrebecq, J. F. (2015). Improvement of the mechanical performances of concrete cylinders confined actively or passively by means of SMA wires. Archives of Civil and Mechanical Engineering, 15(1), 292–299. doi:10.1016/j.acme.2014.04.009.

[41] Cusson, D., & Paultre, P. (1994). High- Strength Concrete Columns Confined by Rectangular Ties. Journal of Structural Engineering, 120(3), 783–804. doi:10.1061/(asce)0733-9445(1994)120:3(783).

[42] Shin, M., & Andrawes, B. (2010). Experimental investigation of actively confined concrete using shape memory alloys. Engineering Structures, 32(3), 656–664. doi:10.1016/j.engstruct.2009.11.012.

[43] Saatcioglu, M., & Razvi, S. R. (1992). Strength and Ductility of Confined Concrete. Journal of Structural Engineering, 118(6), 1590–1607. doi:10.1061/(asce)0733-9445(1992)118:6(1590).

[44] Richart, F. E., Brandtzaeg, A., & Brown, R. L. (1928). A study of the failure of concrete under combined compressive stresses. Engineering Experiment Station. Bulletin; no. 185, University of Illinois, Champaign, United States.

[45] Mander, J. B., Priestley, M. J. N., & Park, R. (1988). Theoretical Stress- Strain Model for Confined Concrete. Journal of Structural Engineering, 114(8), 1804–1826. doi:10.1061/(asce)0733-9445(1988)114:8(1804).

[46] Lim, J. C., & Ozbakkaloglu, T. (2014). Stress-strain model for normal- and light-weight concretes under uniaxial and triaxial compression. Construction and Building Materials, 71, 492–509. doi:10.1016/j.conbuildmat.2014.08.050.

[47] Fardis, M. N., & Khalili, H. H. (1982). FRP-encased concrete as a structural material. Magazine of Concrete Research, 34(121), 191–202. doi:10.1680/macr.1982.34.121.191.

[48] Zhang, B., Yang, Y., & Xia, Z. (2021). Axial Compressive Performance of Concrete Column Reinforced by Prestressed Steel Strips. Bulletin of the Chinese Ceramic Society, 40(7), 2200–2208. doi:10.16552/j.cnki.issn1001-1625.2021.07.003.

[49] Pan, Y., Rui, G., Li, H., Tang, H., & Xu, L. (2017). Study on stress-strain relation of concrete confined by CFRP under preload. Engineering Structures, 143, 52–63. doi:10.1016/j.engstruct.2017.04.004.

[50] Qu, D. C., & Chang, W. (2024). Peak stress and peak strain evaluation of concrete columns confined with lateral ties under axial compression by artificial neural networks. Soft Computing, 28(6), 5591–5608. doi:10.1007/s00500-023-09357-5.

[51] Cascardi, A., Micelli, F., & Aiello, M. A. (2017). An Artificial Neural Networks model for the prediction of the compressive strength of FRP-confined concrete circular columns. Engineering Structures, 140, 199–208. doi:10.1016/j.engstruct.2017.02.047.

[52] Li, S., Zheng, W., Xu, T., & Wang, Y. (2022). Artificial neural network model for predicting the local compression capacity of stirrups-confined concrete. Structures, 41, 943–956. doi:10.1016/j.istruc.2022.05.055.

[53] Yan, F., Lin, Z., Wang, X., Azarmi, F., & Sobolev, K. (2017). Evaluation and prediction of bond strength of GFRP-bar reinforced concrete using artificial neural network optimized with genetic algorithm. Composite Structures, 161, 441–452. doi:10.1016/j.compstruct.2016.11.068.

[54] Raza, A., El Ouni, M. H., Baili, J., & uz Zaman Khan, Q. (2022). Data-driven analysis on axial strength of GFRP-NSC columns based on practical artificial neural network tool. Composite Structures, 291, 115598. doi:10.1016/j.compstruct.2022.115598.

[55] Yuan, Z., Niu, M. Q., Ma, H., Gao, T., Zang, J., Zhang, Y., & Chen, L. Q. (2023). Predicting mechanical behaviors of rubber materials with artificial neural networks. International Journal of Mechanical Sciences, 249, 108265. doi:10.1016/j.ijmecsci.2023.108265.

[56] Bahrami, B., Talebi, H., Ayatollahi, M. R., & Khosravani, M. R. (2023). Artificial neural network in prediction of mixed-mode I/II fracture load. International Journal of Mechanical Sciences, 248, 108214. doi:10.1016/j.ijmecsci.2023.108214.

[57] Ma, Y., Mi, J., Yang, X., Sun, Z., & Liu, C. (2024). Prediction model and sensitivity analysis of ultimate drift ratio for rectangular reinforced concrete columns failed in flexural-shear based on BP-Garson algorithm. Structures, 60, 105808. doi:10.1016/j.istruc.2023.105808.

Appendix I

Table A1. Data of actively confined concrete columns

Reference	Column size (mm)	Concrete strength (MPa)	Spacing (mm)	Number of layers	Prestress level	N_u (kN)	N_c (kN)	N_c/N_u
[48]	400×1000	C20	150	1	2.5×10-3	3903	3313	0.849
	400×1000	C20	150	3	2.5×10-3	4020	4433	1.103
	400×1000	C20	100	1	2.5×10-3	4233	3434	0.811
	400×1000	C20	100	3	2.5×10-3	5178	4793	0.926
	300×750	C20	150	1	2.5×10-3	2362	1922	0.814
	300×750	C20	150	3	2.5×10-3	2460	2667	1.084
	300×750	C20	100	1	2.5×10-3	2070	2028	0.980
	300×750	C20	100	2	2.5×10-3	2802	2507	0.895
	300×750	C20	100	3	2.5×10-3	3706	2985	0.805
	400×1000	C30	150	1	2.5×10-3	4204	4674	1.112
	400×1000	C30	150	2	2.5×10-3	4606	5233	1.136
	400×1000	C30	100	1	2.5×10-3	4356	4794	1.101
	400×1000	C30	100	2	2.5×10-3	4958	5474	1.104
	400×1000	C30	50	1	2.5×10-3	5170	5015	0.970
	400×1000	C30	50	2	2.5×10-3	6850	5916	0.864
	300×750	C30	150	1	2.5×10-3	2752	2687	0.976
	300×750	C30	150	2	2.5×10-3	2846	3059	1.075
	300×750	C30	100	1	2.5×10-3	2755	2793	1.014
	300×750	C30	100	2	2.5×10-3	2983	3059	1.026
	300×750	C30	75	1	2.5×10-3	2434	2867	1.178
	300×750	C30	75	2	2.5×10-3	3447	3419	0.992
	300×750	C30	75	3	2.5×10-3	4515	3970	0.879
	300×750	C30	50	1	2.5×10-3	3235	2979	0.921
	300×750	C30	50	2	2.5×10-3	4017	3643	0.907
	300×750	C30	50	3	2.5×10-3	5263	4307	0.818
[49]	110×200	C20	0	1	0.22	347	300	0.863
	110×200	C20	0	1	0.32	342	307	0.896
	110×200	C20	0	1	0.43	334	314	0.941
	110×200	C20	0	1	0.52	324	321	0.990
	110×200	C20	0	1	0.64	313	329	1.051
	110×200	C20	0	1	0.71	297	334	1.124
	110×200	C20	0	2	0.23	512	447	0.874
	110×200	C20	0	2	0.31	502	459	0.914
	110×200	C20	0	2	0.41	488	473	0.969
	110×200	C20	0	2	0.54	471	491	1.042
	110×200	C20	0	2	0.61	446	501	1.123
	110×200	C30	0	1	0.24	392	356	0.908
	110×200	C30	0	1	0.34	387	363	0.938
	110×200	C30	0	1	0.44	379	370	0.976
	110×200	C30	0	1	0.56	370	378	1.023
	110×200	C30	0	1	0.62	358	382	1.068
	110×200	C30	0	1	0.72	341	389	1.142
	110×200	C30	0	2	0.23	569	502	0.883
	110×200	C30	0	2	0.35	558	519	0.930
	110×200	C30	0	2	0.46	542	535	0.986
	110×200	C30	0	2	0.54	524	546	1.042
	110×200	C30	0	2	0.63	501	558	1.115